

Temperature-mediated transition from Dyakonov–Tamm surface waves to surface-plasmon-polariton waves

Francesco Chiadini¹, Vincenzo Fiumara², Tom G. Mackay^{3,4}, Antonio Scaglione¹, and Akhlesh Lakhtakia⁴

¹Department of Industrial Engineering, University of Salerno, via Giovanni Paolo II, 132 – Fisciano (SA), 84084, Italy;

²School of Engineering, University of Basilicata, Viale dell’Ateneo Lucano 10, 85100 Potenza, Italy;

³School of Mathematics and Maxwell Institute for Mathematical Sciences, University of Edinburgh, Edinburgh EH9 3FD, UK;

⁴Department of Engineering Science and Mechanics, Pennsylvania State University, University Park, PA 16802–6812, USA

Abstract

The effect of changing the temperature on the propagation of electromagnetic surface waves (ESWs), guided by the planar interface of a homogeneous isotropic temperature-sensitive material (namely, InSb) and a temperature-insensitive structurally chiral material (SCM) was numerically investigated in the terahertz frequency regime. As the temperature rises, InSb transforms from a dissipative dielectric material to a dissipative plasmonic material. Correspondingly, the ESWs transmute from Dyakonov–Tamm surface waves into surface–plasmon–polariton waves. The effects of the temperature change are clearly observed in the phase speeds, propagation distances, angular existence domains, multiplicity, and spatial profiles of energy flow of the ESWs. Remarkably large propagation distances can be achieved; in such instances the energy of an ESW is confined almost entirely within the SCM. For certain propagation directions, simultaneous excitation of two ESWs with (i) the same phase speeds but different propagation distances or (ii) the same propagation distances but different phase speeds are also indicated by our results.

Keywords: Dyakonov–Tamm surface wave, surface–plasmon–polariton wave, structurally chiral material, InSb, terahertz regime

1 Introduction

The propagation of any electromagnetic surface wave (ESW) is guided by the planar interface of two different mediums [1, 2]. Uller proved theoretically in 1903 that the two different mediums can be isotropic and homogeneous dielectric materials, the relative permittivities of both partnering materials being positive real, so long as at least one of the two is dissipative.

The prediction was theoretically confirmed shortly thereafter, first by Zenneck [4] and then by Sommerfeld [5–7], and experimentally during this decade [8].

A major development came in 1977, when ESWs were theoretically predicted to exist at the interface of two isotropic dielectric materials [9], at least one of which is periodically nonhomogeneous in the direction normal to the interface. These ESWs were named Tamm waves as they are analogous to the electronic states predicted to exist at the surface of a crystal by Tamm in 1932 [10]. Tamm waves have been experimentally observed [11], and even applied for sensing purposes [12–15].

If the periodically nonhomogeneous partnering material is anisotropic, the ESWs are called Dyakonov–Tamm (DT) surface waves [16]. The periodic nonhomogeneity may be either piecewise homogeneous or continuous. As an example, a Reusch pile [17–21] supports DT surface-wave propagation [22]. This material is piecewise homogeneous as it is a stack of anisotropic dielectric layers with an incremental rotation from one layer to the next about an axis normal to the layers. An equichiral Reusch pile has only two layers per period, whereas an ambichiral Reusch pile has more than two layers per period [23]. If the number of layers per period is sufficiently large, the Reusch pile is classified as finely chiral. A very finely chiral Reusch pile may be regarded as a structurally chiral material (SCM) [24–27] whose nonhomogeneity is effectively continuous.

The allowed directions of propagation in the interface plane define the angular existence domain (AED) of ESWs. The AED of DT surface waves is often so large as to encompass the entire interface plane. In contrast, if the anisotropic and periodically nonhomogeneous partnering material were to be made homogeneous, the AED shrinks to a few degrees in width, if that [28, 29]. Hence, DT surface waves are expected to be exploited for several applications including optical sensing [30]. Furthermore, the multiplicity of DT surface waves that can be excited at a specific frequency for a given propagation direction — as predicted by theory [16] and later observed in experimental studies [31, 32] — is very appealing because it can enhance the sensitivity as well as the reliability of sensing and also allow for the simultaneous detection of multiple analytes.

The temperature dependence of the relative permittivity ε_{th} of certain isotropic dielectric materials, e.g., InSb in the terahertz frequency regime, allows them to change from slightly dissipative dielectric materials (i.e., $\text{Re}(\varepsilon_{th}) > 0$) to plasmonic materials (i.e., $\text{Re}(\varepsilon_{th}) < 0$) or *vice versa*, with the transition occurring at a temperature for which $\text{Re}(\varepsilon_{th}) = 0$ [33]. If such a homogeneous material were to partner a Reusch pile or a SCM, then DT surface waves could be transformed into surface-plasmon-polariton (SPP) waves [2, 34, 35], or *vice versa*.

SPP waves are guided by the planar interface of a plasmonic material (often, a metal at optical frequencies) and a dielectric material that can be either isotropic [34] or anisotropic [36] and either homogeneous [34] or periodically nonhomogeneous [2]. Due to their widespread exploitation for optical sensing [37, 38], SPP waves have an extensive literature. SPP waves also have applications for near-field microscopy [39, 40], harvesting solar energy [41, 42], and communications [43]. In AED and multiplicity, SPP waves and DT surface waves have similar characteristics [2, 44].

In this paper, we focus on the transmutation of DT surface waves into SPP waves when a critical change in temperature transmutes the homogeneous partnering material (InSb) from a dissipative dielectric material to a dissipative plasmonic material, the nonhomogeneous anisotropic partnering material being an SCM. In Sec. 2, we briefly present the theoretical preliminaries for the canonical boundary-value problem that describes ESWs guided by the planar interface of the two chosen materials. Comprehensive details of the solution procedure are presented elsewhere [16, 46–48]. In Sec. 3 we report on the characteristics of the excited ESWs in terms of their wavenumbers, phase speeds, propagation distances, AEDs, and spatial profiles of the time-averaged Poynting vector. By comparing the characteristics of the ESWs when $\text{Re}(\varepsilon_{th})$ for InSb is positive and negative, we characterize the features of the transmutation from DT surface waves to SPP waves. Conclusions follow in Sec. 4.

An $\exp(-i\omega t)$ dependence on time t is implicit, with ω denoting the angular frequency and $i = \sqrt{-1}$. The free-space wavenumber, the free-space wavelength, and the intrinsic impedance of free space are denoted by $k_0 = \omega\sqrt{\varepsilon_0\mu_0}$, $\lambda_0 = 2\pi/k_0$, and $\eta_0 = \sqrt{\mu_0/\varepsilon_0}$, respectively, with ε_0 and μ_0 being the permeability and permittivity of free space. The speed of light in free space is denoted by $c_0 = 1/\sqrt{\varepsilon_0\mu_0}$. Vectors are in boldface; dyadics are underlined twice; and Cartesian unit vectors are identified as $\hat{\mathbf{u}}_x$, $\hat{\mathbf{u}}_y$, and $\hat{\mathbf{u}}_z$.

2 Theoretical Preliminaries

In order to investigate temperature-sensitive ESW propagation guided by the planar interface of InSb (or a similar homogeneous material) and a SCM, we formulated a canonical boundary-value problem, and thereby obtained a dispersion equation that was numerically solved.

A schematic of the canonical boundary-value problem is provided in Fig. 1. The half space $z < 0$ is occupied by a homogeneous and isotropic material, namely InSb, whose relative permittivity ε_{th} varies with temperature in a known way. The half space $z > 0$ is occupied by a SCM which is assumed to be a unidirectionally nonhomogeneous material, characterized by constitutive parameters that vary continuously and periodically along the z direction [27]. This macroscopic assumption is valid provided that the length scale of the SCM's morphology is considerably smaller than the electromagnetic wavelengths involved. By a process of local homogenization [27], the macroscopic description can be inferred from the underlying nanostructure of the SCM [45]. The nonhomogeneous relative permittivity dyadic of the SCM is given by

$$\underline{\underline{\varepsilon}}_{\text{SCM}}(z) = \underline{\underline{S}}_z(z) \cdot \underline{\underline{S}}_y(\chi) \cdot \underline{\underline{\varepsilon}}_{ref}^\circ \cdot \underline{\underline{S}}_y^{-1}(\chi) \cdot \underline{\underline{S}}_z^{-1}(z), \quad (1)$$

with the dyadic

$$\underline{\underline{\varepsilon}}_{ref}^\circ = \varepsilon_a \hat{\mathbf{u}}_z \hat{\mathbf{u}}_z + \varepsilon_b \hat{\mathbf{u}}_x \hat{\mathbf{u}}_x + \varepsilon_c \hat{\mathbf{u}}_y \hat{\mathbf{u}}_y \quad (2)$$

indicating local orthorhombicity. Herein ε_a , ε_b , and ε_c are complex-valued, ω -dependent, parameters whose values are assumed to be independent of temperature. The ω -independent

rotation and tilt dyadics

$$\left. \begin{aligned} \underline{\underline{S}}_z(z) &= (\hat{\mathbf{u}}_x \hat{\mathbf{u}}_x + \hat{\mathbf{u}}_y \hat{\mathbf{u}}_y) \cos(\pi z / \Omega) \\ &\quad + h (\hat{\mathbf{u}}_y \hat{\mathbf{u}}_x - \hat{\mathbf{u}}_x \hat{\mathbf{u}}_y) \sin(\pi z / \Omega) + \hat{\mathbf{u}}_z \hat{\mathbf{u}}_z \\ \underline{\underline{S}}_y(\chi) &= (\hat{\mathbf{u}}_x \hat{\mathbf{u}}_x + \hat{\mathbf{u}}_z \hat{\mathbf{u}}_z) \cos \chi \\ &\quad + (\hat{\mathbf{u}}_z \hat{\mathbf{u}}_x - \hat{\mathbf{u}}_x \hat{\mathbf{u}}_z) \sin \chi + \hat{\mathbf{u}}_y \hat{\mathbf{u}}_y \end{aligned} \right\} \quad (3)$$

together delineate the SCM's helicoidal morphology with $h = 1$ denoting structural right-handedness and $h = -1$ structural left-handedness, 2Ω is the structural period of the SCM along the z axis, and $\chi \in (0, \pi/2]$. Both partnering materials are assumed to have unit relative permeability.

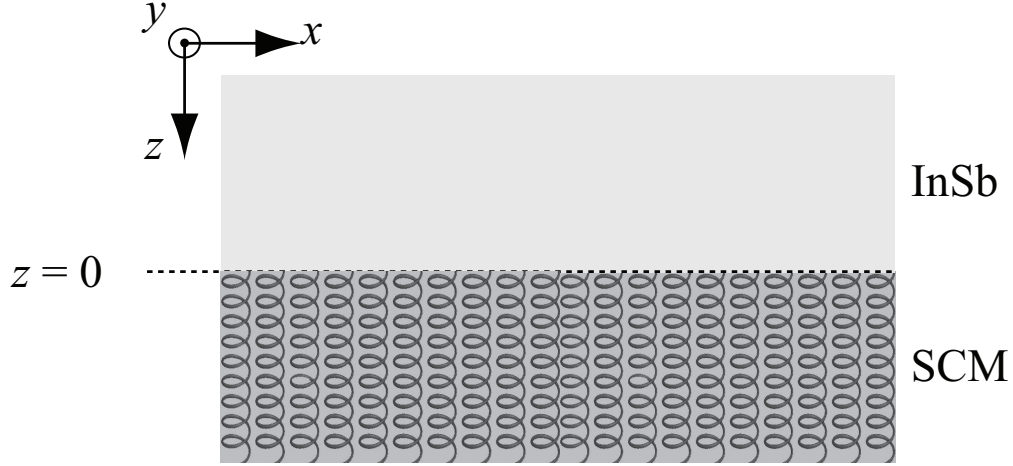


Figure 1: Schematic of the canonical boundary-value problem solved.

We consider the ESW to be propagating parallel to the unit vector $\hat{\mathbf{u}}_{prop} = \hat{\mathbf{u}}_x \cos \psi + \hat{\mathbf{u}}_y \sin \psi$, $\psi \in [0, 2\pi)$, in the xy plane. The magnitudes of the field phasors of the ESW decay to zero as $z \rightarrow \pm\infty$. With q as the wavenumber, the electric and magnetic phasors of the ESW can be represented everywhere by

$$\left. \begin{aligned} \mathbf{E}(\mathbf{r}) &= \mathbf{e}(z) \exp(iq\hat{\mathbf{u}}_{prop} \cdot \mathbf{r}) \\ \mathbf{H}(\mathbf{r}) &= \mathbf{h}(z) \exp(iq\hat{\mathbf{u}}_{prop} \cdot \mathbf{r}) \end{aligned} \right\} \quad (4)$$

where \mathbf{r} is the position vector. Appropriate representations of the amplitude functions $\mathbf{e}(z)$ and $\mathbf{h}(z)$ in the half spaces $z < 0$ and $z > 0$, and the derivation of the corresponding dispersion relation and subsequent extraction of q therefrom, are comprehensively described elsewhere [2, 16, 46–48]. For each value of ψ , the dispersion relation may yield multiple values of q .

3 Numerical Results and Discussion

We numerically solved the dispersion relation to obtain the normalized wavenumbers $\tilde{q} = q/k_0$ of the ESWs. Once q (or \tilde{q}) is known, the corresponding propagation length and phase

speed of the ESW were calculated as $\Delta_{prop} = 1/\text{Im}(q)$ and $v_{ph} = c_0/\text{Re}(\tilde{q})$, respectively. The spatial profile of the rate of energy flow associated with an ESW is provided via the time-averaged Poynting vector $\mathbf{P}(\mathbf{r}) = (1/2) \text{Re}[\mathbf{e}(z) \times \mathbf{h}^*(z)] \exp[-2\text{Im}(q)\hat{\mathbf{u}}_{prop} \cdot \mathbf{r}]$, where the asterisk denotes the complex conjugate. For all numerical results reported here, we fixed $\lambda_0 = 500 \mu\text{m}$ and $\Omega = 200 \mu\text{m}$, while the direction of propagation was varied in the entire xy plane.

The partnering material occupying the half-space $z < 0$ was taken to be the semiconductor InSb, whose relative permittivity in the terahertz regime is given by the Drude model [33, 49]

$$\varepsilon_{th} = \varepsilon_\infty - \frac{\omega_p^2}{\omega^2 + i\gamma\omega}, \quad (5)$$

wherein the high-frequency relative permittivity $\varepsilon_\infty = 15.68$, the damping constant $\gamma = \pi \times 10^{11} \text{ rad s}^{-1}$, and the plasma frequency $\omega_p = \sqrt{Nq_e^2/0.015\varepsilon_0 m_e}$ depends upon the electronic charge $q_e = -1.60 \times 10^{-19} \text{ C}$ and mass $m_e = 9.11 \times 10^{-31} \text{ kg}$. The dependence of ε_{th} on temperature T (in K) is mediated by the intrinsic carrier density (in m^{-3}) [50–52]

$$N = 5.76 \times 10^{20} T^{3/2} \exp\left(-\frac{E_g}{2k_B T}\right), \quad (6)$$

with $E_g = 0.26 \text{ eV}$ being the band-gap energy and $k_B = 8.62 \times 10^{-5} \text{ eV K}^{-1}$ being the Boltzmann constant. Whereas $\varepsilon_{th} = 10.95 + 0.39i$ at $T = 180 \text{ K}$, $\varepsilon_{th} = -13.66 + 2.44i$ at $T = 220 \text{ K}$. Thus, InSb is a dissipative dielectric material at $T = 180 \text{ K}$ but a metal at $T = 220 \text{ K}$, with $\text{Re}(\varepsilon_{th}) = 0$ at $T \approx 204.56 \text{ K}$. The constitutive parameters of the SCM were chosen to be $\varepsilon_a = 1.574$, $\varepsilon_b = 3.228$, $\varepsilon_c = 2.313$, $\chi = 20^\circ$, and $h = 1$.

3.1 Wavenumbers and propagation distances

Figures 2 and 3, respectively, show the real part of the normalized wavenumber \tilde{q} and the propagation distance Δ_{prop} for all solutions of the dispersion relation, as the angle ψ of the direction of propagation in the xy plane is varied from 0 to 2π , with $T = 180 \text{ K}$ fixed. The solutions were organized into two sets each composed by three different branches numbered 1 to 3, and 1' to 3', respectively. If q is a solution for a specific value of the propagation angle ψ on branch ℓ , it is also a solution for either $\psi + \pi$ or $\psi - \pi$ on branch ℓ' . This symmetry arises from that of $\varepsilon_{\text{SCM}}(z)$ in the xy plane.

All branches in Figs. 2 and 3 span limited ranges of ψ that in some cases overlap, either partially or totally. These overlaps indicate the multiplicity of DT surface waves for the ranges of ψ involved. For any propagation angle, the interface guides at least two DT surface waves. Furthermore, as many as four DT surface waves can propagate in the intervals $0 \leq \psi \leq 0.1333\pi$ and $1 \leq \psi \leq 1.1333\pi$, both of which are highlighted in gray in Figs. 2 and 3.

As the propagation angle ψ increases, the value of $\text{Re}(\tilde{q})$ in Figs. 2 increase on branches 1, 2, 1', and 2'. The same is also true on branch 3 for $\psi < 1.1111\pi$ and on branch 3' for $\psi < 0.1111\pi$ and $\psi > 0.994\pi$, with $\text{Re}(\tilde{q})$ slightly decreasing as ψ increases for $1.1111\pi <$

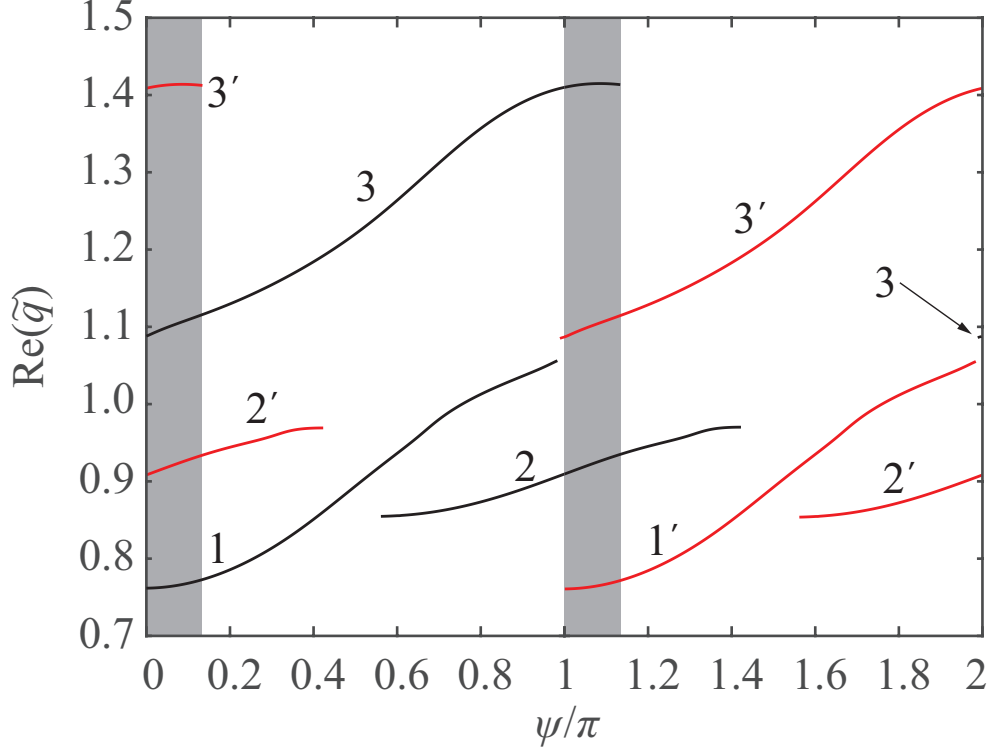


Figure 2: Variation of $\text{Re}(\tilde{q})$ with ψ of DT surface waves guided by the planar InSb/SCM interface at $T = 180$ K ($\varepsilon_{th} = 10.95 + 0.39i$). The solutions of the dispersion equation are organized in 6 numbered branches. Ranges of ψ with four ESWs are shaded gray in Figs. 2–5, 8, and 9.

$\psi < 1.133\pi$ on branch 3 and for $0.1111\pi < \psi < 0.133\pi$ on branch 3'. The phase speeds of the DT surface waves on branches 2 and 2', on branch 1 for $0 \leq \psi < 0.7556\pi$, and on branch 1' for $1 \leq \psi < 1.7556\pi$ are higher than the speed of light in vacuum (i.e., $v_{ph} > c_0$). In contrast, the phase speeds of the DT surface waves on branches 3 and 3', on branch 1 for $0.7556 < \psi \leq 0.9830\pi$, and on branch 1' for $1.7556 < \psi \leq 1.9830\pi$ are lower than the speed of light in vacuum (i.e., $v_{ph} < c_0$).

At six different values of ψ , two branches intersect in Fig. 3 but not in Fig. 2. Consequently, for each of the six intersections in Fig. 3, a pair of DT surface waves can be simultaneously excited with the same attenuation rates in the interface plane but with different phase speeds.

Data on AEDs, relative phase speeds, and propagation distances are reported in Table 1. The maximum value of Δ_{prop} in this table is a phenomenally large 9.95 m on branches 2 and 2' — two orders of magnitude greater than the maximum propagation distances on any of the other branches.

The real part of the normalized wavenumber and the propagation distance, respectively, are presented in Figs. 4 and 5 as ψ/π varies for ESWs guided by the planar InSb/SCM interface when $T = 200$ K. These ESWs are classified as DT surface waves because $\varepsilon_{th} =$

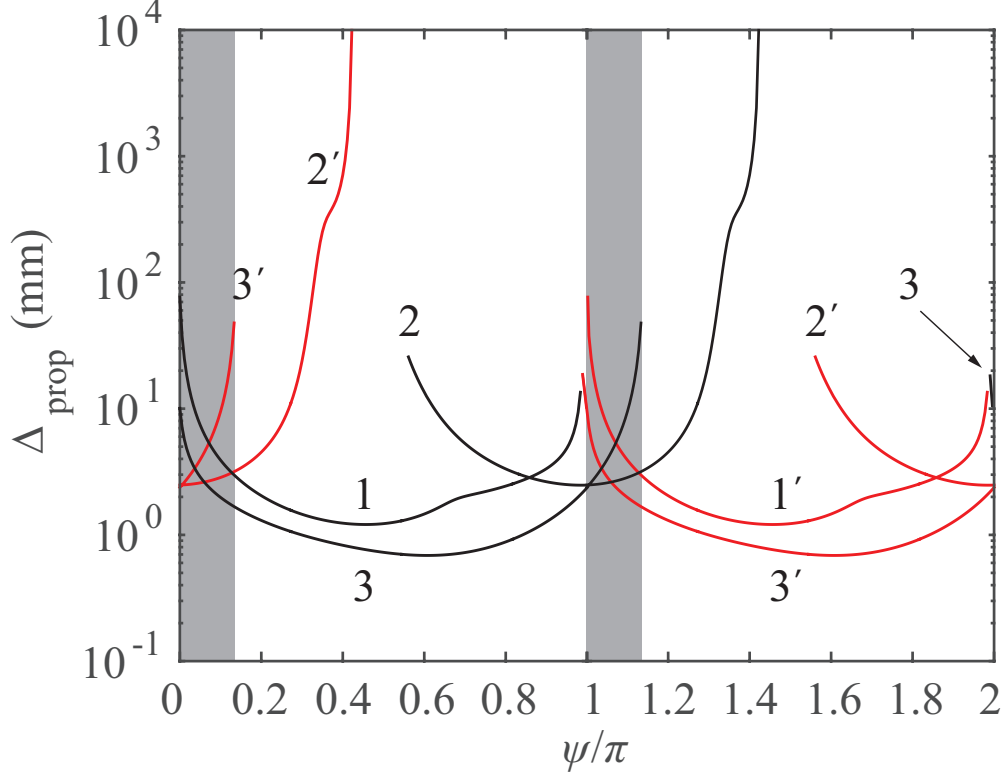


Figure 3: As Fig. 2 but the variation of Δ_{prop} is presented.

$2.87 + 1.07i$. A comparison with Figs. 2 and 3 reveals that increasing the temperature by 20 K does not affect the number of solution branches, there being six solution branches at 200 K. The branches are numbered from 1 to 3 and from 1' to 3'. If q is a solution for a specific value of ψ on branch ℓ , it is also a solution for either $\psi + \pi$ or $\psi - \pi$ on branch ℓ' .

All six branches at $T = 200$ K cover limited ranges of ψ . Except for branches 3 and 3' for which $\text{Re}(\tilde{q})$ decreases as the propagation angle ψ increases, no monotonic trend can be recognized in the other branches. On branches 1 and 1', on branch 2 for $0.444\pi \leq \psi < 1.289\pi$, and on branch 2' for $0 \leq \psi < 0.289\pi$ and $1.444 \leq \psi \leq 2\pi$, the phase speeds exceed c_0 ; in contrast, $v_{ph} < c_0$ on branch 2 for $1.289 < \psi \leq 1.978\pi$, and on branch 2' for $0.289 < \psi \leq 0.978\pi$, as well as on branches 3 and 3'.

The overlaps of different branches results in a multiplicity of DT surface waves that can be as high as four, depending upon ψ . The four ranges where the maximum multiplicity of DT surface waves arises ($0.444\pi \leq \psi \leq 0.589\pi$, $0.7\pi \leq \psi \leq 0.978\pi$, $1.444\pi \leq \psi \leq 1.589\pi$, and $1.7\pi \leq \psi \leq 1.978\pi$) are highlighted in gray in Figs. 4 and 5.

Figure 4 reveals an interesting phenomenon. Branches 1' and 2' intersect at $\psi = 0.2232\pi$ and $\psi = 1.8855\pi$, whereas branches 1 and 2 intersect at $\psi = 0.8855\pi$ and $\psi = 1.2232\pi$. None of the four intersections is found in Fig. 5. Hence, at each of the four values of ψ identified, two DT surface waves can be simultaneously excited with the same phase speeds but different attenuation rates in the interface plane.

Table 1: Angular existence domain, minimum and maximum values of relative phase speed v_{ph}/c_0 , and minimum and maximum values of propagation distance Δ_{prop} for DT surface waves guided by the InSb/SCM interface when $T = 180$ K.

Branch	AED (ψ/π)	$v_{ph}^{(min)}/c_0$	$v_{ph}^{(max)}/c_0$	$\Delta_{prop}^{(min)}$ (mm)	$\Delta_{prop}^{(max)}$ (mm)
1	[0, 0.983]	0.9468	1.3127	1.21	76.52
1'	[1, 1.983]	0.9468	1.3127	1.21	76.52
2	[0.561, 1.422]	1.0308	1.1700	2.48	9947.18
2'	[0, 0.422] \cup [1.561, 2]	1.0308	1.1700	2.48	9947.18
3	[0, 1.133] \cup [1.994, 2]	0.7093	0.9198	0.69	19.40
3'	[0, 0.133] \cup [0.994, 2]	0.7093	0.9198	0.69	19.40

Two branches intersect at ten different values of ψ in Fig. 5. None of those ten intersections are evident in Fig. 4. Hence, at each of ten intersections in Fig. 5, a pair of DT surface waves can be simultaneously excited with the same attenuation rates in the interface plane but with different phase speeds.

Data on AEDs, relative phase speeds, and propagation distances at $T = 200$ K are provided in Table 2. The maximum propagation distance on branches 1 and 1' is a remarkably large 7.96 m.

Table 2: Angular existence domain, minimum and maximum values of normalized phase speed v_{ph}/c_0 , and minimum and maximum values of propagation distance Δ_{prop} for DT surface waves guided by the InSb/SCM interface when $T = 200$ K.

Branch	AED (ψ/π)	$v_{ph}^{(min)}/c_0$	$v_{ph}^{(max)}/c_0$	$\Delta_{prop}^{(min)}$ (mm)	$\Delta_{prop}^{(max)}$ (mm)
1	[0, 0.033] \cup [0.700, 2]	1.0259	1.4388	0.56	7957.75
1'	[0, 1.033] \cup [1.700, 2]	1.0259	1.4388	0.56	7957.75
2	[0.444, 1.978]	0.6830	1.3162	0.19	38.44
2'	[0, 0.978] \cup [1.444, 2]	0.6830	1.3162	0.19	38.44
3	[0.372, 0.589]	0.9147	0.9461	9.69	1326.29
3'	[1.372, 1.589]	0.9147	0.9461	9.69	1326.29

Figures 6 and 7 show the variations of $\text{Re}(\tilde{q})$ and Δ_{prop} , respectively, with ψ when $T = 205$ K. The increment of 5 K from 200 K results in the sign of $\text{Re}(\varepsilon_{th})$ changing from positive to negative, with $\text{Re}(\varepsilon_{th}) = 0$ occurring at $T \approx 204.56$ K. Since InSb changes from being a dissipative dielectric material to a dissipative plasmonic material, a comparison of Figs. 4 and 5 on the one hand with Figs. 6 and 7 on the other hand reveals the effects of the transition from DT surface waves to SPP waves. The number of solution branches increases from six (numbered 1 to 3 and 1' to 3') at 200 K to nine (numbered 1 to 5, 1', 2', 4', and 5') at 205 K. If q is a solution for a particular value of ψ , it is also a solution for $\psi \pm \pi$.

The propensity for multiple solutions of the dispersion equation enhances with the temperature rising to 205 K, with as many as five SPP waves existing in four angular ranges:

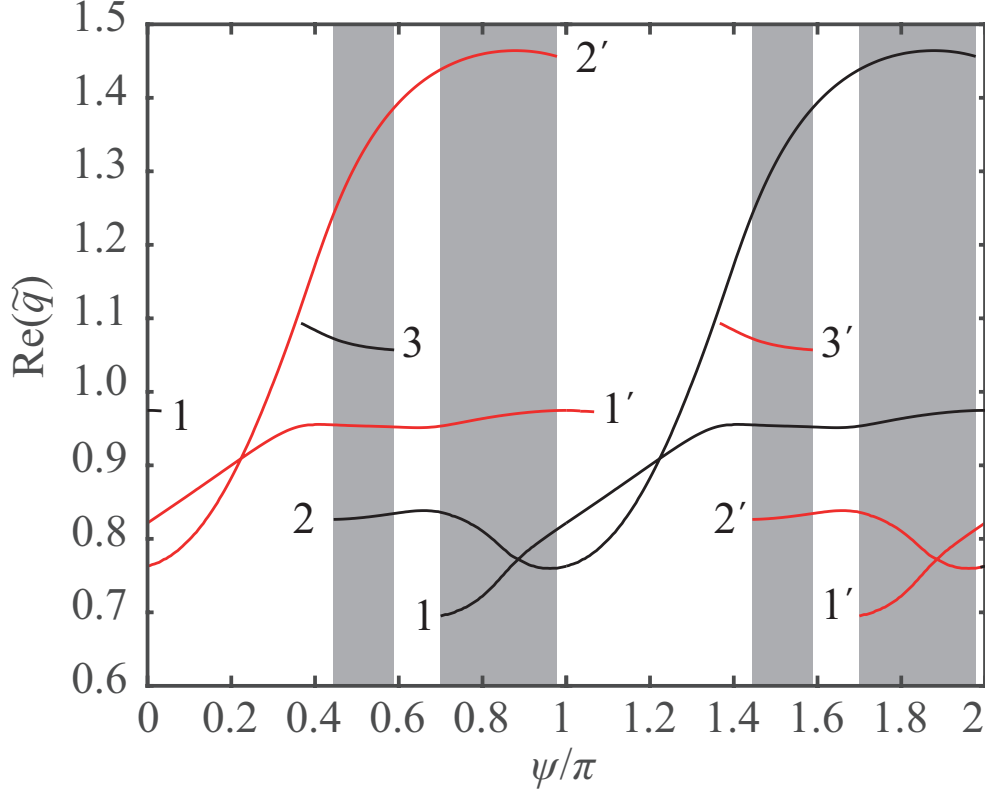


Figure 4: As Fig. 2 except that $T = 200$ K ($\varepsilon_{th} = 2.87 + 1.07i$).

$0.361\pi \leq \psi \leq 0.383\pi$, $0.622\pi \leq \psi \leq 0.739\pi$, $1.361\pi \leq \psi \leq 1.383\pi$, and $1.622\pi \leq \psi \leq 1.739\pi$. In contrast to the case for $T = 200$ K and $T = 180$ K, when $T = 205$ K one branch (namely, branch 3) spans the entire angular range $0 \leq \psi < 2\pi$.

Two SPP waves can be simultaneously excited at 205 K with the same phase speed but not identical propagation distances at: (i) $\psi = 0.143\pi$ where branches 1' and 3 intersect, (ii) $\psi = 0.6978\pi$ where branches 2 and 3 intersect, (iii) $\psi = 1.143\pi$ where branches 1 and 3 intersect and (iv) $\psi = 1.6978\pi$ where branches 2' and 3 intersect. For 18 values of $\psi \in [0, 2\pi)$, a pair of SPP waves can be simultaneously excited with the same attenuation rates in the interface plane but with different phase speeds.

SPP-wave propagation on branches 1, 1', 2, 2', 3, 4 for $0.311\pi \leq \psi \leq 0.482\pi$, and 4' for $1.311\pi \leq \psi \leq 1.482\pi$ in Fig. 6 occurs with $v_{ph} > c_0$. Phase speeds lower than the speed of light in free space are associated with SPP waves on branch 4 for $0.482\pi \leq \psi \leq 0.739\pi$, branch 4' for $1.482\pi \leq \psi \leq 1.739\pi$, 5, and 5'. As revealed in Fig. 7, $\Delta_{prop} > 2$ mm for every branch except branch 3. Moreover, as ψ increases, branch 3 at 205 K shows nearly constant values of Δ_{prop} .

Data on AEDs, relative phase speeds, and propagation distances at $T = 205$ K are provided in Table 3. The longest propagation distances are at least one order magnitude less than they are for $T = 180$ and 200 K. In fact, the longest propagation distance at $T = 205$ K

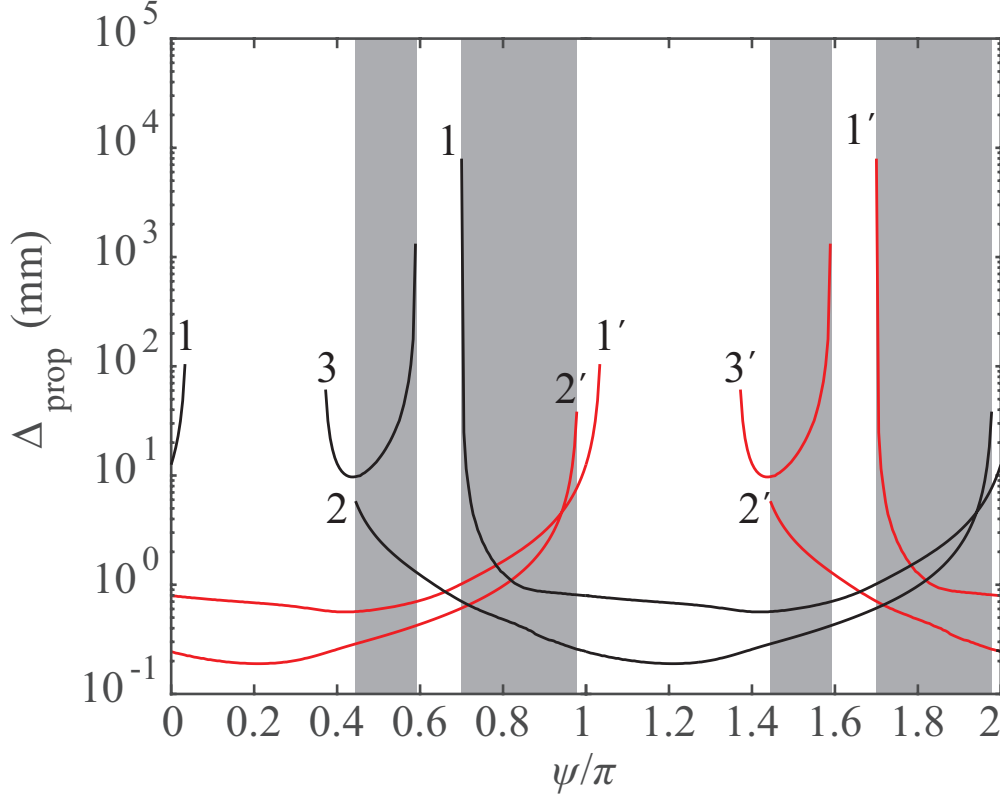


Figure 5: As Fig. 3 except that $T = 200$ K ($\varepsilon_{th} = 2.87 + 1.07i$).

is 416.64 mm, which arises on branches 4 and 4'.

Lastly, $\text{Re}(\tilde{q})$ and Δ_{prop} are plotted in Figs. 8 and 9 as functions of ψ for $T = 220$ K. If q is a solution for a particular value of ψ , it is also a solution for $\psi \pm \pi$. A comparison with Figs. 6 and 7 reveals that an increase in the temperature from 205 K to 220 K results in the number of solution branches increasing to 12. These branches are labeled 1 to 6 and 1' to 6'. None of these branches spans the entire range of ψ .

In spite of the increase in the number of solution branches at $T = 220$ K, the maximum multiplicity of SPP waves is four, which arises for six angular ranges: $0.272\pi \leq \psi \leq 0.278\pi$, $0.539\pi \leq \psi \leq 0.589\pi$, $0.6\pi \leq \psi \leq 0.789\pi$, $1.272\pi \leq \psi \leq 1.278\pi$, $1.539\pi \leq \psi \leq 1.589\pi$, and $1.6\pi \leq \psi \leq 1.789\pi$. As ψ increases, $\text{Re}(\tilde{q})$ increases for all branches. SPP waves on branches 1, 1', 2, 2', 3, 3', 4 for $0.539 \leq \psi \leq 0.632\pi$, and on branch 4' for $1.539 \leq \psi \leq 1.632\pi$ in Fig. 8 have phase speeds greater than the speed of light in vacuum.

No intersections of branches can be seen in Fig. 8. Therefore, it is not possible to excite two SPP waves with the same phase speed for propagation in any specific direction in the interface plane, when $T = 220$ K. For 22 values of $\psi \in [0, 2\pi)$, a pair of SPP waves can be simultaneously excited with the same attenuation rates in the interface plane but, of course, with different phase speeds.

Data on AEDs, relative phase speeds, and propagation distances at 220 K are provided

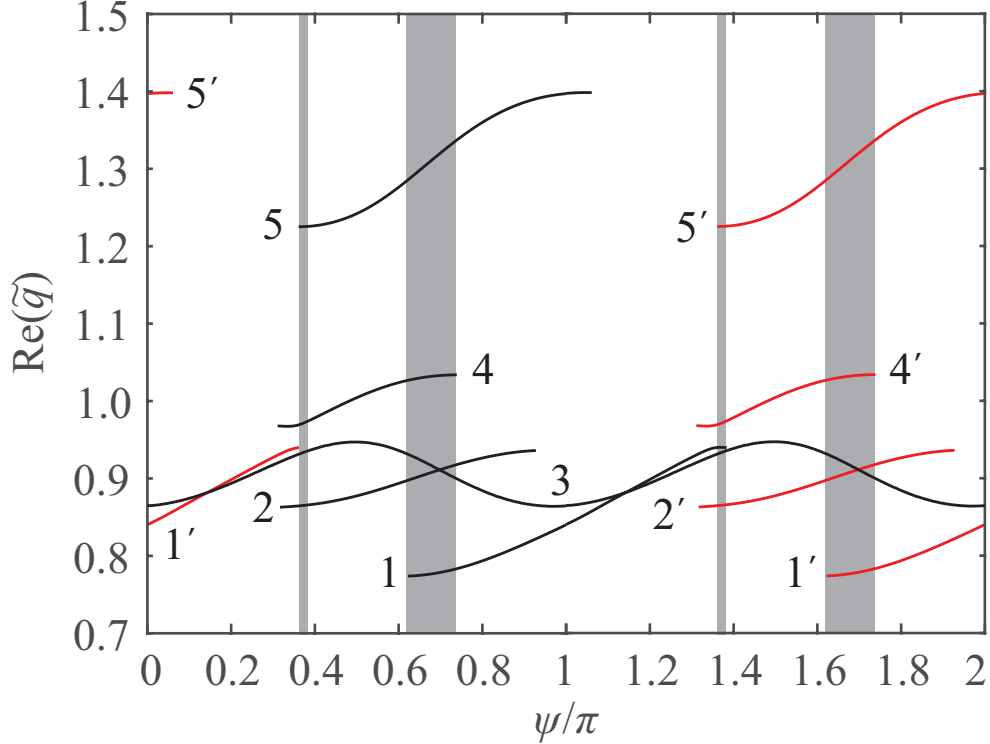


Figure 6: As Fig. 2 except that $T = 205$ K ($\varepsilon_{th} = -0.30 + 1.33i$). Ranges of ψ with 5 SPP waves are shaded gray.

in Table 4. Long-range propagation of SPP waves is possible at 220 K, with the highest value 8.74 m of Δ_{prop} arising on branches 5 and 5'.

3.2 Power profiles

In order to further illuminate the characteristics of the ESWs, we plotted the Cartesian components of $\mathbf{P}(0, 0, z)$ along the z axis. As an illustrative example, Fig. 10 presents the spatial profile of $\mathbf{P}(0, 0, z)$ for the DT surface wave on branch 2' for $\psi = 0.422\pi$ when $T = 180$ K. This ESW has the longest propagation distance (9.95 m) for all investigations reported in this paper. The energy of the DT surface wave exists almost entirely in the half space occupied by the SCM; i.e., the magnitude of $\mathbf{P}(0, 0, z)$ is very small for $z \in (-1, 0]$ mm, and vanishingly small for $z < -1$ mm. The spatial periodicity of the SCM is reflected in the plots of the x and y components of $\mathbf{P}(0, 0, z)$ for $z > 0$. Also, the DT surface wave in the SCM decays so slowly that 50 SCM periods are needed to bring about an appreciable decay of $\mathbf{P}(0, 0, z)$ in the half space $z > 0$.

Figures 11 and 12 present the spatial profile of $\mathbf{P}(0, 0, z)$ for the SPP waves on branches 2 and 3, respectively, for $\psi = 0.6978\pi$ when $T = 205$ K. At this value of ψ , branches 2 and 3 intersect in Fig. 6. The differences in their spatial profiles is striking even though both SPP waves have the same phase speed.

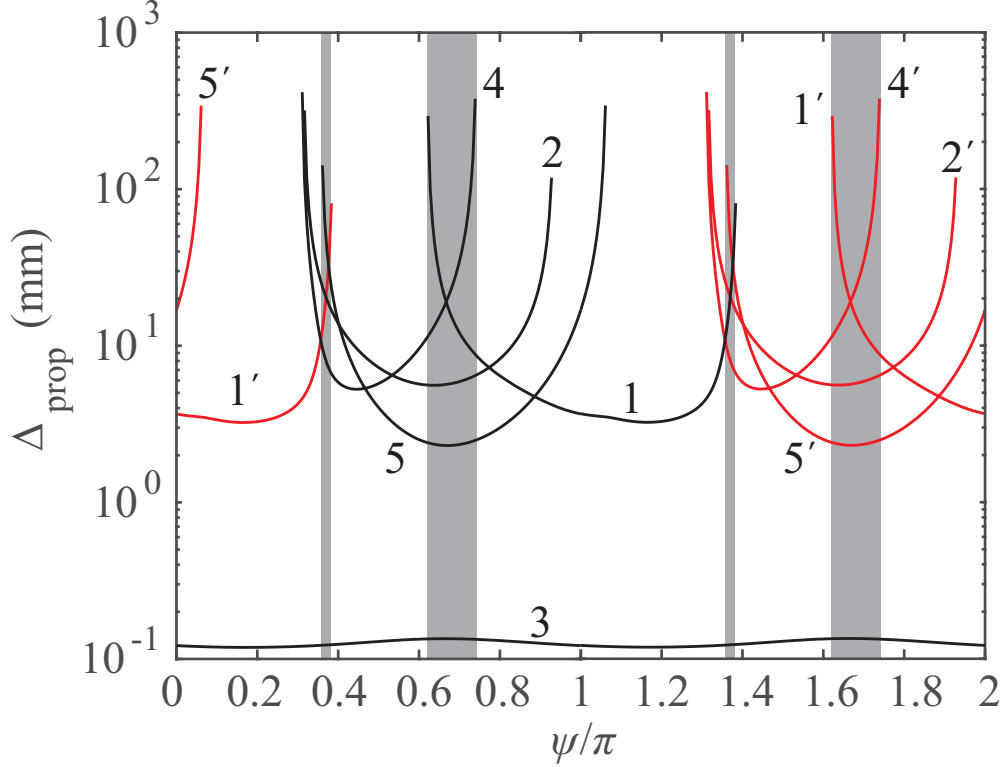


Figure 7: As Fig. 6 but the variation of Δ_{prop} is presented.

In Fig. 11, the SPP wave exists almost entirely in the half space occupied by the SCM; i.e., the magnitude of $\mathbf{P}(0, 0, z)$ is negligible for $z < 0$ relative to that for $z > 0$. Approximately 10 SCM periods are needed in order for the fields to decay appreciably in the half space $z > 0$.

In contrast, the energy of the SPP wave is distributed across both the InSb material and the SCM in Fig. 12. The components of $\mathbf{P}(0, 0, z)$ in Fig. 12 decay more rapidly in the SCM than they do in Fig. 11. Indeed, the amplitude of $\mathbf{P}(0, 0, z)$ in Fig. 12 decays appreciably in only one SCM period in the $z > 0$ half space. As the energy of the SPP wave is squeezed into much less space in Fig. 12 as compared to Fig. 11, the maximum amplitudes of $\mathbf{P}(0, 0, z)$ are much greater (about 100 mW/m²) in Fig. 12 as compared to Fig. 11. Also, the plots of the x and y components of $\mathbf{P}(0, 0, z)$ for $z > 0$ in Fig. 12 do not display high-frequency fluctuations, which contrasts starkly with the corresponding plots in Figs. 10 and 11.

From Figs. 11 and 12, it may be inferred that for SPP waves with phase speed greater than c_0 , some SPP waves are much more tightly bound to the interface than others. To explore this issue further, we turn to Fig. 13 wherein the Cartesian components of $\mathbf{P}(0, 0, z)$ are plotted along the z axis for the following cases involving $v_{ph} \leq c_0$ for both DT surface waves and SPP waves. Fig. 13(a) corresponds to the branch-2 solution in Figs. 4 and 5 at $\psi = 1.1444\pi$. Since $T = 200$ K, the ESW is a DT surface wave. Here $\tilde{q} = 0.8301 + i0.4087$. The corresponding phase speed is $v_{ph} = 1.2047c_0$ and the DT surface wave is tightly bound to the interface.

Table 3: Angular existence domain, minimum and maximum values of normalized phase speed v_{ph}/c_0 , and minimum and maximum values of propagation distance Δ_{prop} for SPP waves guided by the InSb/SCM interface when $T = 205$ K.

Branch	AED (ψ/π)	$v_{ph}^{(min)}/c_0$	$v_{ph}^{(max)}/c_0$	$\Delta_{prop}^{(min)}$ (mm)	$\Delta_{prop}^{(max)}$ (mm)
1	[0.622, 1.383]	1.0639	1.2922	3.23	293.64
1'	[0, 0.383] \cup [1.622, 2]	1.0639	1.2922	3.23	293.64
2	[0.317, 0.928]	1.0683	1.1589	5.60	318.31
2'	[1.317, 1.928]	1.0683	1.1589	5.60	318.31
3	[0, 2]	1.0559	1.1574	0.12	0.13
4	[0.311, 0.739]	0.9672	1.0338	5.28	416.64
4'	[0.311, 0.739]	0.9672	1.0338	5.28	416.64
5	[0.361, 1.061]	0.7152	0.8162	2.31	341.53
5'	[0, 0.061] \cup [1.361, 2]	0.7152	0.8162	2.31	341.53

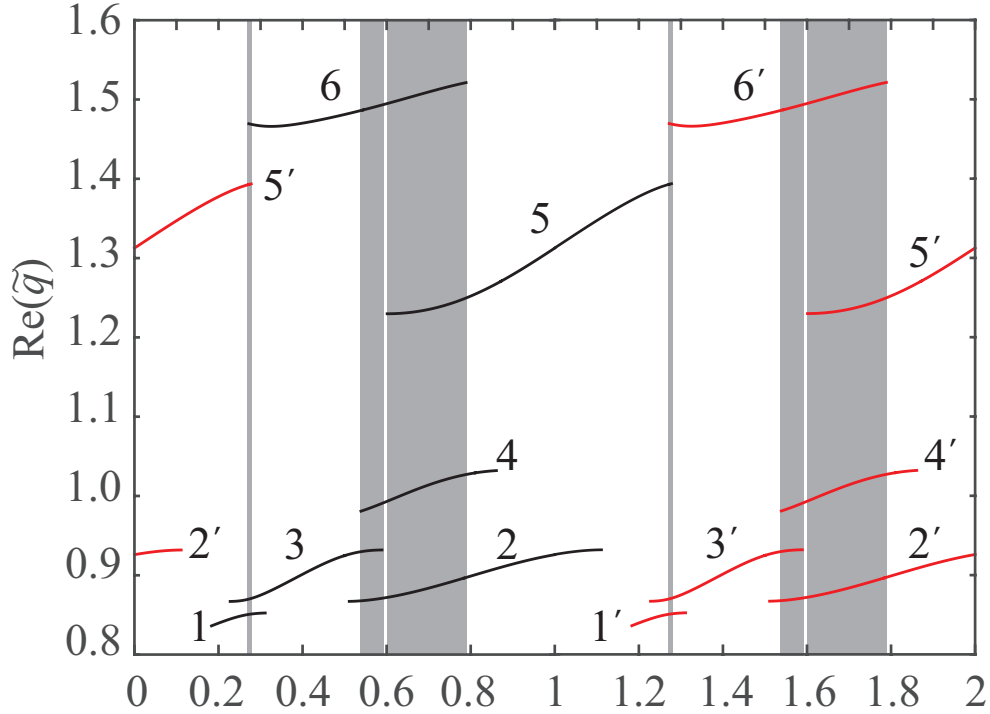


Figure 8: As Fig. 2 except that $T = 220$ K ($\varepsilon_{th} = -13.66 + 2.44i$).

Fig. 13(b) is the same as Fig. 13(a) except for $\psi = 1.4500\pi$. Here $\tilde{q} = 1.2499 + i0.2731$. The corresponding phase speed is $v_{ph} = 0.8000c_0$ and the DT surface wave is tightly bound to the interface. Fig. 13(c) corresponds to the branch 1 solution in Figs. 6 and 7 at $\psi = 0.9722\pi$. Since $T = 205$ K, the ESW is a SPP wave. Here $\tilde{q} = 0.8333 + i0.0208$. The corresponding phase speed is $v_{ph} = 1.2000c_0$ and the SPP wave is loosely bound to the interface. Fig. 13(d)

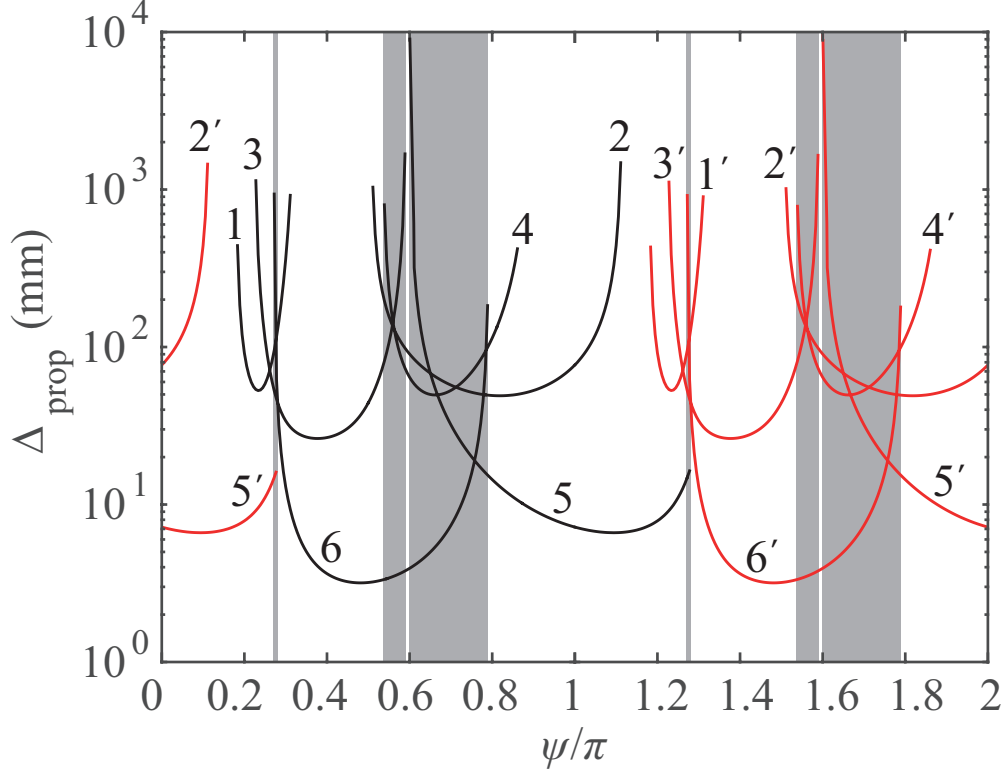


Figure 9: As Fig. 3 except that $T = 220$ K ($\epsilon_{th} = -13.66 + 2.44i$).

corresponds to the branch 5 solution in Figs. 6 and 7 at $\psi = 0.5278\pi$. Since $T = 205$ K, the ESW is a SPP wave. Here $\tilde{q} = 1.24982 + i0.0236$. The corresponding phase speed is $v_{ph} = 0.8000c_0$ and the SPP wave is somewhat loosely bound to the interface.

Judging by Fig. 13, as well as by Figs. 11 and 12, there is no obvious relationship between the extent to which a DT surface wave or a SPP wave is bound to the interface and its phase speed relative to c_0 . However, a relationship is apparent between Δ_{prop} and the extent to which an ESW is bound to the interface. To pursue this further, let us introduce e -folding distances in the InSb half-space and in the SCM half-space, namely Δ_{InSb} and Δ_{SCM} respectively, to characterize the decay of the electric field amplitude of ESWs in the $\pm z$ directions. That is, at a distance Δ_{InSb} from the interface the magnitude of the electric field has decayed by a factor of $1/e$ in the InSb half space, and Δ_{SCM} is similarly defined for the SCM half space. For the numerical examples considered here, every SPP wave that has $\Delta_{prop} \gtrsim 3$ mm, regardless of its phase speed, has a relatively large value of Δ_{InSb} and of Δ_{SCM} and therefore is loosely bound to the interface. The same relationship also holds for DT surface waves that have $\Delta_{prop} \gtrsim 0.5$ mm. Some representative data are presented in Table 5 in support of this finding.

Table 4: Angular existence domain , minimum and maximum values of normalized phase speed v_{ph}/c_o , and minimum and maximum values of propagation distance Δ_{prop} for SPP waves guided by the InSb/SCM interface when $T = 220$ K.

Branch	AED (ψ/π)	$v_{ph}^{(min)}/c_o$	$v_{ph}^{(max)}/c_o$	$\Delta_{prop}^{(min)}$ (mm)	$\Delta_{prop}^{(max)}$ (mm)
1	[0.183, 0.311]	1.1731	1.1959	52.91	918.91
1'	[1.183, 1.311]	1.1731	1.1959	52.91	918.91
2	[0.511, 1.111]	1.0730	1.1533	49.04	1480.62
2'	$[0, 0.111] \cup [1.511, 2]$	1.0730	1.1533	49.04	1480.62
3	[0.228, 0.589]	1.0730	1.1534	26.25	1684.18
3'	[1.228, 1.589]	1.0730	1.1534	26.25	1684.18
4	[0.539, 0.861]	0.9690	1.0195	49.61	799.77
4'	[1.539, 1.861]	0.9690	1.0195	49.61	799.77
5	[0.6, 1.278]	0.7176	0.8132	6.62	8744.78
5'	$[0, 0.278] \cup [1.6, 2]$	0.7176	0.8132	6.62	8744.78
6	[0.272, 0.789]	0.6573	0.6821	3.18	936.21
6'	[1.272, 1.789]	0.6573	0.6821	3.18	936.21

4 Concluding remarks

The effect of changing temperature on the propagation of ESWs guided by the planar interface of InSb and a SCM was numerically investigated in the terahertz frequency regime. On raising the temperature, InSb is transformed from a dissipative dielectric material to a dissipative plasmonic material. Consequently, the ESWs transmute from DT surface waves to SPP waves. The dispersion relation, arising from the solution of a canonical boundary-value problem, can yield multiple values for the wavenumber q for any propagation direction. A multiplicity of ESWs was found. To be specific, for the particular scenarios considered here, as many as four DT surface waves and up to five SPP waves may be excited for certain propagation directions. The propagation distances of some ESWs are remarkably high, reaching in a few cases lengths of some meters; in such instances the energy of the ESW is almost entirely within the SCM. While the foregoing analysis clearly demonstrates that ESWs of a wide variety of different natures can be excited, depending upon temperature, the reasons for this diversity of natures are not revealed. For example, the reasons for the sharp contrast between the power profiles represented in Figs. 11 and 12 for SPP waves at the same temperature and with the same propagation direction are not clear. Further analysis is required to shed light on this matter.

For certain propagation directions, simultaneous excitation of two ESWs with the same phase speeds but different propagation distances is possible. In a similar vein, two ESWs with the same propagation distances but different phase speeds may be simultaneously excited for certain propagation directions. The simultaneous excitation of such ESWs does not infer coupling between those ESWs.

Clearly, the canonical boundary-value problem considered herein, based on two infinite

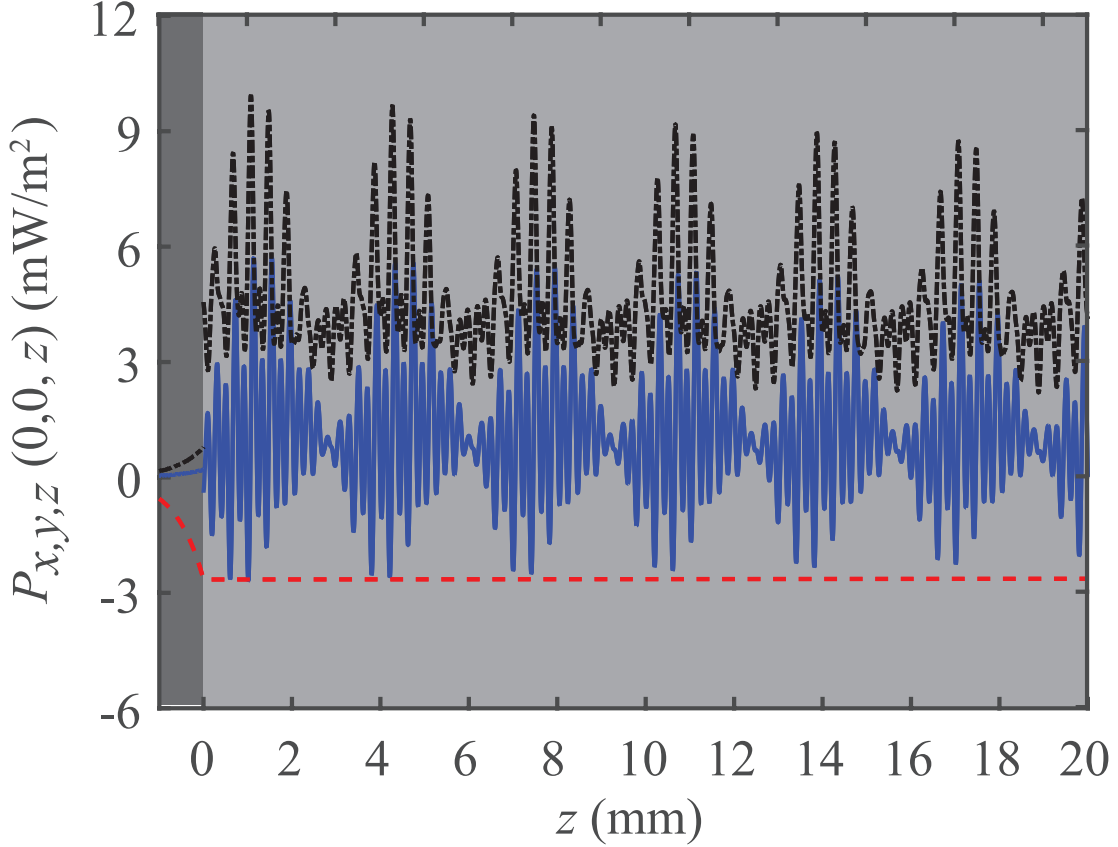


Figure 10: Cartesian components $P_x(0,0,z)$ (blue solid lines), $P_y(0,0,z)$ (black dashed-dotted lines), and $P_z(0,0,z)$ (red dashed lines) of $\mathbf{P}(0,0,z)$ plotted against z for the DT surface wave on branch $2'$ in Figs. 2 and 3. Calculations were made with $\psi = 0.422\pi$ and $T = 180$ K. The normalization protocol for these graphs is explained in a predecessor paper [54]

half spaces, is not practically implementable. However, it provides valuable insights into the essential characteristics of ESW excitation that may be reasonably expected in more realistic scenarios. For example, qualitatively similar surface-wave characteristics may be anticipated for the practically implementable grating-coupled and waveguide-coupled configurations in the case of Dyakonov-Tamm surface waves, as well as for the grating-coupled, waveguide-coupled, and prism-coupled configurations in the case of SPP waves [2].

Acknowledgement. A. Lakhtakia thanks the Charles Godfrey Binder Endowment at the Pennsylvania State University for ongoing support of his research.

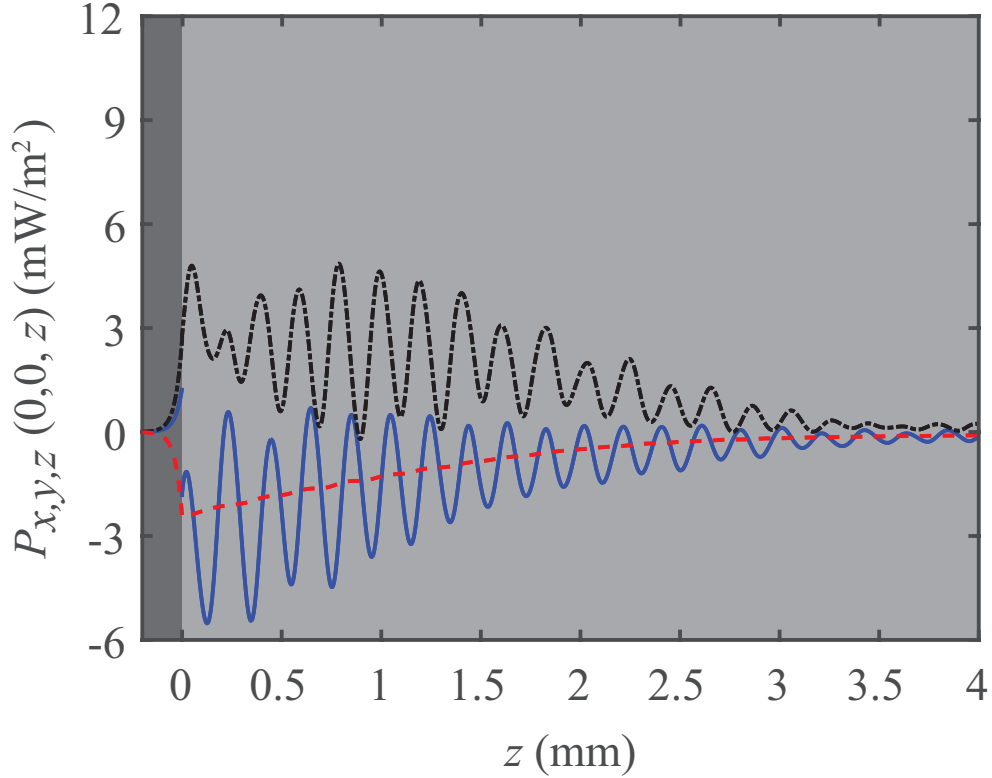


Figure 11: As Fig. 10 except that the Cartesian components of $\mathbf{P}(0, 0, z)$ are plotted against z for the SPP wave on branch 2 in Figs. 6 and 7, when $T = 205$ K and $\psi = 0.6978\pi$.

References

- [1] Boardman A D (ed) 1982 *Electromagnetic Surface Modes* (New York, NY, USA: Wiley)
- [2] Polo J A Jr, Mackay T G, and Lakhtakia A 2013 *Electromagnetic Surface Waves: A Modern Perspective* (Waltham, MA, USA: Elsevier)
- [3] Uller K 1903 *Beiträge zur Theorie der Elektromagnetischen Strahlung* Ph.D. thesis (Rostock, Germany: Universität Rostock), Chap. XIV
- [4] Zenneck J 1907 Über die Fortpflanzung ebener elektromagnetischer Wellen längs einer ebenen Leiterfläche und ihre Beziehung zur drahtlosen Telegraphie *Ann. Phys. Lpz.* **23** 846–866
- [5] Sommerfeld A 1909 Über die Ausbreitung der Wellen in der drahtlosen Telegraphie *Ann. Phys. Lpz.* **28** 665–736
- [6] Sommerfeld A 1920 Über die Ausbreitung der Wellen in der drahtlosen Telegraphie *Ann. Phys. Lpz.* **62** 95–96

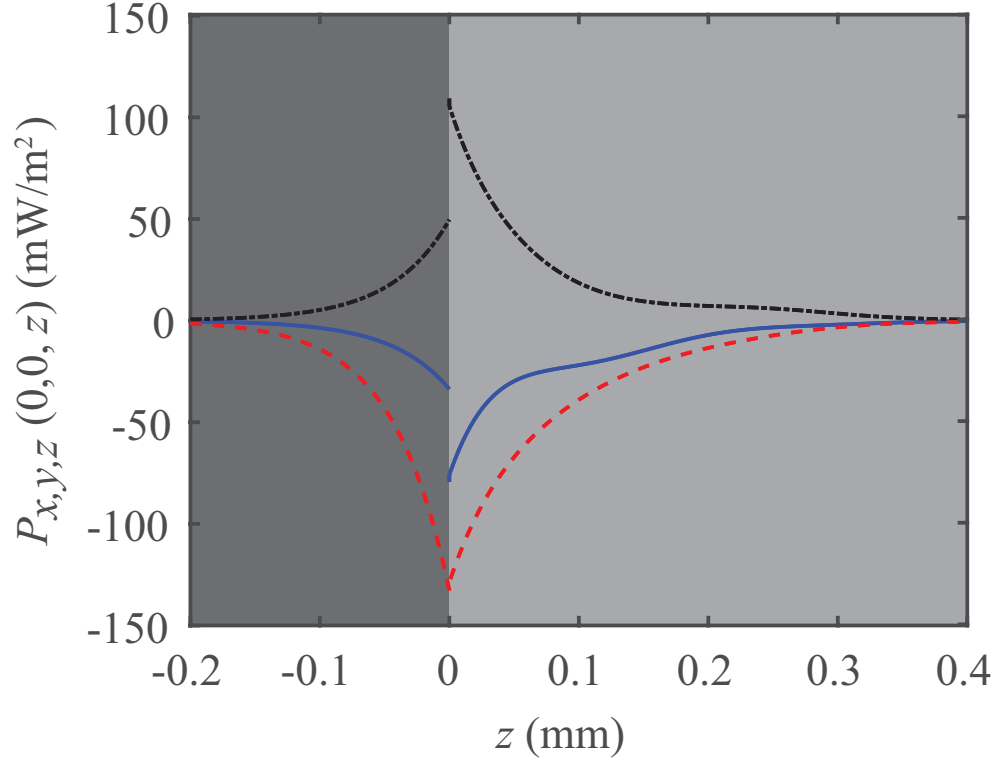


Figure 12: As Fig. 11 except that the Cartesian components of $\mathbf{P}(0, 0, z)$ are plotted against z for the SPP wave on branch 3.

- [7] Sommerfeld A 1926 Über die Ausbreitung der Wellen in der drahtlosen Telegraphie *Ann. Phys. Lpz.* **81** 1135–1153
- [8] Faryad M and Lakhtakia A 2014 Observation of the Uller–Zenneck wave *Opt. Lett.* **39** 5204–5207
- [9] Yeh P, Yariv A, and Hong C S 1977 Electromagnetic propagation in periodic stratified media. I. General theory *J. Opt. Soc. Am.* **67** 423–438
- [10] Tamm I 1932 Über eine mögliche Art der Elektronenbindung an Kristalloberflächen *Z. Phys. A* **76** 849–850
- [11] Yeh P, Yariv A, and Cho A Y 1978 Optical surface waves in periodic layered media *Appl. Phys. Lett.* **32** 104–105
- [12] Shinn M and Robertson W M 2005 Surface plasmon-like sensor based on surface electromagnetic waves in a photonic band-gap material *Sens. Actuat. B: Chem.* **105** 360–364
- [13] Konopsky V N and Alieva E V 2007 Photonic crystal surface waves for optical biosensors *Anal. Chem.* **79** 4729–4735

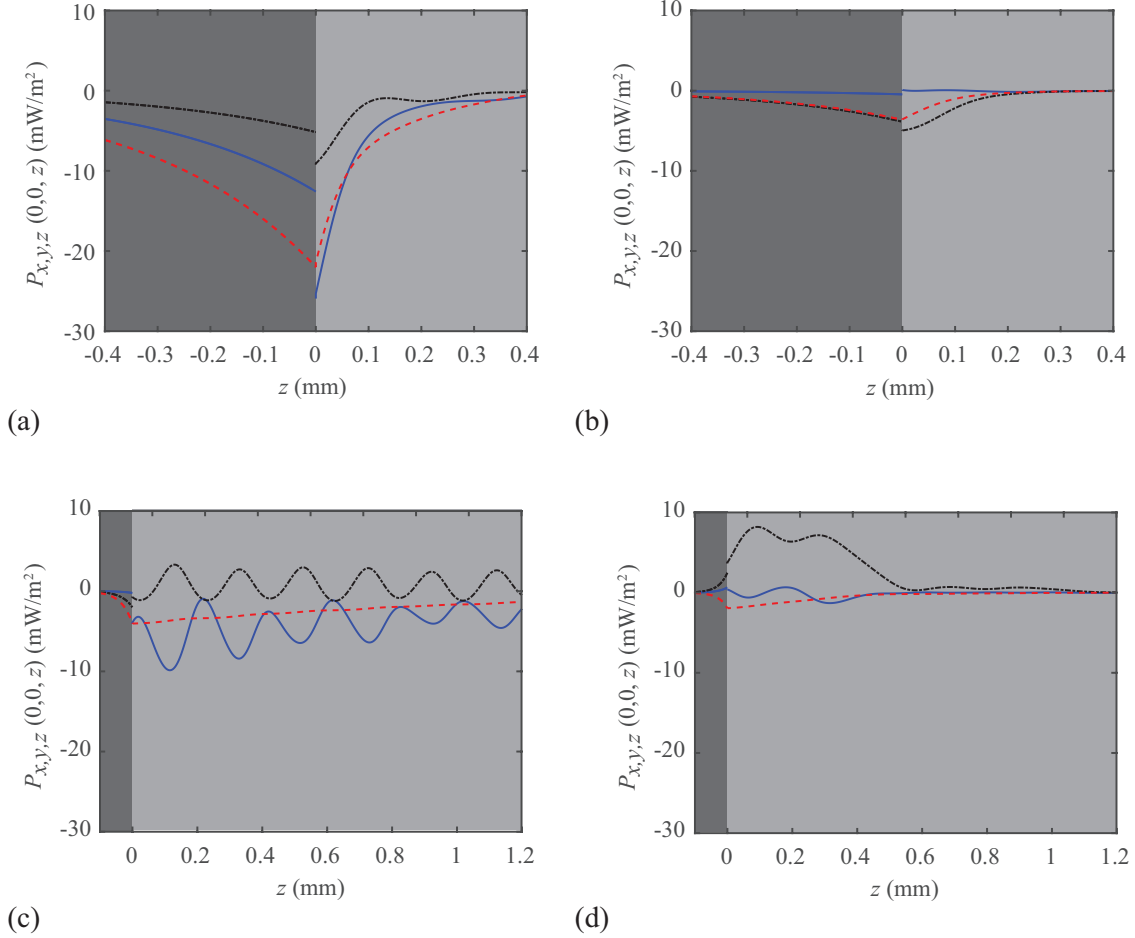


Figure 13: As in Fig. 10, Cartesian components of $\mathbf{P}(0, 0, z)$ plotted against z for $T = 200$ K in (a) and (b) and 205 K in (c) and (d). Further details are provided in the text.

- [14] Sinibaldi A, Danz N, Descrovi E, Munzert P, Schulz U, Sonntag F, Dominici L, and Michelotti F 2012 Direct comparison of the performance of Bloch surface wave and surface plasmon polariton sensors *Sens. Actuat. B: Chem.* **174** 292–298
- [15] Konopsky V N, Karakouz T, Alieva E V, Vicario C, Sekatskii S K, and Dietler G 2013 Photonic crystal biosensor based on optical surface waves *Sensors* **13** 2566–2578
- [16] Lakhtakia A and Polo J A Jr 2007 Dyakonov–Tamm wave at the planar interface of a chiral sculptured thin film and an isotropic dielectric material *J. Eur. Opt. Soc. Rapid Publ.* **2** 07021
- [17] Reusch E 1869 Untersuchung über Glimmercombinationen *Ann. Phys. Chem.* **138** 628–638

Table 5: The e -folding distances Δ_{InSb} and Δ_{SCM} , normalized phase speed v_{ph}/c_0 , propagation distance Δ_{prop} , and ratio $\text{Im}(\tilde{q})/\text{Re}(\tilde{q})$ for a selection of DT surface waves and SPP waves. Further details are provided in the text.

Branch	T (K)	ψ/π	Δ_{InSb} (mm)	Δ_{SCM} (mm)	v_{ph}/c_0	Δ_{prop} (mm)	$\text{Im}(\tilde{q})/\text{Re}(\tilde{q})$
3	180	0.572	4.564	0.289	0.79941	0.69204	0.09192
1	180	0.356	1.740	1.853	1.20005	1.30562	0.07314
2'	200	0.150	0.638	0.257	1.19804	0.19385	0.49179
2'	200	0.450	0.490	0.229	0.80006	0.29139	0.21850
1	205	0.972	0.069	2.215	1.20048	3.82584	0.02497
5	205	0.528	0.056	0.531	0.80012	3.37193	0.01888
5	220	0.789	0.020	0.593	0.80021	15.37967	0.00414
1	220	0.183	0.021	2.825	1.19590	440.55512	0.00022

- [18] Joly G and Billard J 1981 ‘Quelques champs électromagnétiques dans les piles de Reusch I. — Les vibrations propres d’une pile de deux lames a biréfringence rectiligne ne sont pas orthogonales *J. Opt. (Paris)* **12** 323–329
- [19] Joly G and Billard J 1982 Quelques champs électromagnétiques dans les piles de Reusch. II. Piles éclairées sous l’incidence normale par des ondes monochromatiques planes et uniformes *J. Opt. (Paris)* **13** 227–238
- [20] Joly G and Isaert N 1985 Quelques champs électromagnétiques dans les piles de Reusch III. Biréfringence elliptique des vibrations itératives; activité optique de piles hélicoïdales d’extension finie *J. Opt. (Paris)* **16** 203–213
- [21] Joly G and Isaert N 1986 Quelques champs électromagnétiques dans les piles de Reusch IV—Domaines multiples de réflexion sélective *J. Opt. (Paris)* **17** 211–221
- [22] Polo J A Jr and Lakhtakia A 2011 Dyakonov–Tamm waves guided by the planar interface of an isotropic dielectric material and an electro-optic ambichiral Reusch pile *J. Opt. Soc. Am. B* **28** 567–576
- [23] Hodgkinson I J, Lakhtakia A, Wu Q h, De Silva L, and McCall M W 2004 Ambichiral, equichiral and finely chiral layered structures *Opt. Commun.* **239** 353–358
- [24] Bose J C 1898 On the rotation of plane of polarisation of electric waves by a twisted structure *Proc. R. Soc. Lond.* **63** 146–152
- [25] Chandrasekhar S 1992 *Liquid Crystals, 2nd ed.* (Cambridge, United Kingdom: Cambridge University Press)
- [26] De Gennes P G and Prost J A 1993 *The Physics of Liquid Crystals, 2nd ed.* (Oxford, United Kingdom: Clarendon Press)

- [27] Lakhtakia A and Messier R 2005 *Sculptured Thin Films: Nanoengineered Morphology and Optics* (Bellingham, WA, USA: SPIE Press)
- [28] Takayama O, Crasovan L-C, Johansen S K, Mihalache D, Artigas D, and Torner L 2008 Dyakonov surface waves: A review *Electromagnetics* **28** 126–145
- [29] Takayama O, Crasovan L, Artigas D, and Torner L 2009 Observation of Dyakonov surface waves *Phys. Rev. Lett.* **102** 043903
- [30] Lakhtakia A and Faryad M 2014 Theory of optical sensing with Dyakonov–Tamm waves *J. Nanophoton.* **8** 083072
- [31] Pulsifer D P, Faryad M, and Lakhtakia A 2013 Observation of the Dyakonov–Tamm wave *Phys. Rev. Lett.* **111** 243902
- [32] Pulsifer D P, Faryad M, Lakhtakia A, Hall A S, and Liu L 2013 Experimental excitation of the Dyakonov–Tamm wave in the grating-coupled configuration *Opt. Lett.* **39** 2125–2128
- [33] Howells S C and Schlie L A 1996 Transient terahertz reflection spectroscopy of undoped InSb from 0.1 to 1.1 THz *Appl. Phys. Lett.* **69** 550–552
- [34] Pitarke J M, Silkin V M, Chulkov E V, and Echenique P M 2007 Theory of surface plasmon and surface-plasmon polaritons *Rep. Prog. Phys.* **70** 1–87
- [35] Maier S 2006 *Plasmonics: Fundamentals and Applications* (Heidelberg, Germany: Springer)
- [36] Sprokel G J 1981 The reflectivity of a liquid crystal cell in a surface plasmon experiment *Mol. Cryst. Liq. Cryst.* **68** 39–45
- [37] Homola J (ed) 2006 *Surface Plasmon Resonance Based Sensors* (Heidelberg, Germany: Springer)
- [38] Swiontek S E and Lakhtakia A 2016 Influence of silver-nanoparticle layer in a chiral sculptured thin film for surface-multiplasmonic sensing of analytes in aqueous solution *J. Nanophoton.* **10** 033008
- [39] Campbell C T and Kim G 2007 SPR microscopy and its applications to high-throughput analyses of biomolecular binding events and their kinetics *Biomaterials* **28** 2380–2392
- [40] Kawata S, Inouye Y, and Verma P 2009 Plasmonics for near-field nano-imaging and superlensing *Nat. Photon.* **3** 388–394
- [41] Mokkaapati S and Catchpole K R 2012 Nanophotonic light trapping in solar cells *J. Appl. Phys.* **112** 101101

- [42] Anderson T H, Faryad M, Mackay T G, Lakhtakia A, and Singh R 2016 Combined optical-electrical finite-element simulations of thin-film solar cells with homogeneous and nonhomogeneous intrinsic layers *J. Photon. Energy* **6** 025502
- [43] Sekhon J S and Verma S S 2011 Plasmonics: the future wave of communication *Curr. Sci.* **101** 484–488
- [44] Chiadini F, Fiumara V, Scaglione A, and Lakhtakia A 2016 Compound guided waves that mix characteristics of surface-plasmon-polariton, Tamm, Dyakonov–Tamm, and Uller–Zenneck waves *J. Opt. Soc. Am. B* **33** 1197–1206
- [45] Mackay T G and Lakhtakia A 2012 Modeling chiral sculptured thin films as platforms for surface-plasmonic-polaritonic optical sensing *IEEE Sensors J.* **12** 273–280
- [46] Polo J A Jr and Lakhtakia A 2009 On the surface plasmon polariton wave at the planar interface of a metal and a chiral sculptured thin film *Proc. R. Soc. Lond. A* **465** 87–107
- [47] Chiadini F, Fiumara V, Scaglione A, and Lakhtakia A 2015 Composite surface-plasmon-polariton waves guided by a thin metal layer sandwiched between a homogeneous isotropic dielectric material and a periodically multi-layered isotropic dielectric material *J. Nanophoton.* **9** 093060
- [48] Chiadini F, Fiumara V, Scaglione A, and Lakhtakia A 2016 Compound surface-plasmon-polariton waves guided by a thin metal layer sandwiched between a homogeneous isotropic dielectric material and a structurally chiral material *Opt. Commun.* **363** 201–206
- [49] Han J and Lakhtakia A 2009 Semiconductor split-ring resonators for thermally tunable terahertz metamaterials *J. Modern Opt.* **56** 554–557
- [50] Cunningham R W and Gruber J B 1970 Intrinsic concentration and heavy-hole mass in InSb *J. Appl. Phys.* **41** 1804–1809
- [51] Oszwaldowski M and Zimpel M 1988 Temperature dependence of intrinsic carrier concentration and density of states effective mass of heavy holes in InSb *J. Phys. Chem. Solids* **49** 1179–1185
- [52] Halevi P and Ramos-Mendieta F 2000 Tunable photonic crystals with semiconducting constituents *Phys. Rev. Lett.* **85** 1875–1878
- [53] Mackay T G and Lakhtakia A 2016 Temperature-mediated transition from Dyakonov surface waves to surface-plasmon-polariton waves *IEEE Photon. J.* **8** 4802813
- [54] Chiadini F, Fiumara V, Mackay T G, Scaglione A, and Lakhtakia A 2016 Left/right asymmetry in Dyakonov–Tamm-wave propagation guided by a topological insulator and a structurally chiral material, *J. Opt. (UK)* **18** 115101